FULL RESEARCH ARTICLE

In-situ dispersion hardened aluminum bronze/steel composites prepared using a double wire electron beam additive manufacturing

Anna Zykova[1] · Aleksandr Panfilov[1] · Andrey Chumaevskii[1] · Andrey Vorontsov[1] · Evgeny Moskvichev[1] ·
Sergey Nikonov[1] · Denis Gurianov[1] · Nickolai Savchenko[1] · Evgeny Kolubaev[1] · Sergei Tarasov[1]

Abstract

Electron beam additive manufacturing with simultaneously controlled feeding and melting of ER321 stainless steel and CuA19Mn2 bronze wires was carried out. The composite microstructure was formed consisting of homogeneously distributed ferrite and nickel-enriched bronze grains. Intensive intermixing and diffusion in the melted pool caused redistribution of nickel from stainless steel to the bronze and solidification of ferrite grains instead of the austenitic ones. Dispersion hardening of both ferrite and aluminum bronze grains occurred by core/shell β′/AlNi and AlFe$_3$ (κ$_{iv}$-phase) precipitates, respectively, that resulted in improving the ultimate tensile stress and increasing the microhardness of the composites depending upon the content of stainless steel introduced. Deformation was localized mainly in the bronze grains while ferrite grains retained their shape and were almost free of dislocations. The bronze grains allowed revealing only small regions containing the deformation microtwins. The tensile strength and microhardness of the composite samples were increased as compared to those of the pure bronze. No anisotropy was found during tensile testing.

Keywords Electron beam additive manufacturing · In-situ composite · Phase transformation · Dispersion hardening

1 Introduction

Additive manufacturing is a rapidly developing trend in almost all the industries including even such traditional ones as construction [1]. However, the fabrication of metallic components is still the most demanded application of these methods. Despite many alloys and composites are fabricated using traditional metallurgy or powder production methods, the additive manufacturing offers new solutions for in-situ controlling and modifying the alloy or composite structures. One of such solutions may be simultaneous additive deposition of dissimilar metals that would allow in-situ forming an alloy or a composite.

The steel/bronze composite materials can be fabricated using different methods including smelting-casting, brazing, welding, jet binding or plasma-transferred arc deposition [2–6] that would allow obtaining products with properties combining good processability with high corrosion resistance or strength and toughness with high heat- and electric conductivities.

Aluminum bronzes that contain up to 12 wt% of Al and additionally alloyed by Fe, Ni or Mn are widely used in various applications that require combined properties [7, 8]. The functional characteristics of the aluminum bronzes are determined by the microstructures formed in them in accordance with the process used. Along with that chemical composition of the bronzes determines the phase transformations that may occur in these alloys including for example, ordering [9, 10] or formation of intermetallic compounds [11] under corresponding conditions.

For instance, Tao et al. showed that phases formed in the Fe and Ni containing aluminum bronze coating obtained by laser-assisted deposition were as follows: α-Cu, γ$_2$, β′, Cr-Fe and κ-phase [11]. The content of Cr-Fe increased with the addition of Fe and Ni and resulted in the α-Cu grain refining, increasing the microhardness and improving wear resistance.

Increasing contents of both Ni and Cr allowed enhancing hardness and corrosion resistance of the aluminum bronzes [12, 13]. Chromium is known as a good corrosion inhibitor but it is hardly possible to dissolve more than 1 at.% Cr in

✉ Anna Zykova
zykovaap@mail.ru

1   Institute of Strength Physics and Materials Science
    Siberian Branch of Russian Academy of Sciences, 2/4,
    Akademichesky Ave., Tomsk 634055, Russia

Cu applying the standard metallurgical melting. Instead, the bronze surface may be alloyed with Cr by means of friction stir processing, ion implantation, magnetron sputtering, etc. For instance, the improved corrosion resistance of a nickel-aluminum bronze was achieved by ion implantation of Cr atoms into its subsurface [14].

An austenitic stainless steel possesses high strength and corrosion resistance and therefore is a good candidate for dispersing in a bronze matrix and thus improving its strength and wear resistance. This type of composites can be used for replacing the costly rare-earth element containing alloys as well as for reducing costs and weight of the composites.

Deposition of a nickel aluminum bronze on a stainless steel by means of wire arc additive manufacturing (WAAM) was undertaken and allowed obtaining a bimetallic sample with FeAl intermetallic layer (IMC) as well as containing the κ_I –precipitates in the bronze layer [14]. Multilayer aluminum bronze/stainless steel structures were obtained using laser metal deposition to reduce the detrimental effects of IMCs formed at the interface between layers [15].

Additive laser directed energy deposition (DED) manufacturing of a multimaterial composed of nickel aluminum bronze and steel layers was carried out [16] where bronze layers were embrittled by the formed martensite and IMCs such as Fe_3Al and NiAl. Nevertheless, such an approach allowed improving the corrosion resistance of the bronze.

Plasma-transferred arc (PTA) process was used for deposition of a Cu–Al–Fe coating on the EN10503 steel substrate and studying the effect of dilution on the resulting coating's microstructure [2]. The amount of κ-phase precipitates was depending on the amount of Fe admixed to the bronze. An attempt was undertaken to densify the porous jet-printed stainless steel 420 parts by pre-sintering and infiltration with a bronze that resulted in embrittlement of the steel samples [3].

Electron beam wire-feed additive manufacturing (EBAM) has a high potential for fabricating bimetallic and even multimetallic materials since this process involves local fusion binding between successively deposited dissimilar metal layers. The necessity of using a vacuum chamber may be justified by achieving the zero porosity in the samples grown. Stainless steel/copper composites were prepared using the double wire feed EBAM [17] when a gradient concentration transition zone was obtained with a variety of structures and lack of nickel dissolution in copper. On the contrary, additive deposition of a laminate composite with alternating steel and copper layers allowed observing the nickel depletion zones in the vicinity of the Cu/steel boundaries [17].

Additive manufacturing with the use of aluminum bronze wire showed that columnar oriented grains grow from the bottom of the electron beam melted pool [18] that have detrimental effect on the mechanical strength of the grown metal wall. Post-processing by pre-deformation and subsequent

annealing allowed improving mechanical characteristics of the metal [19]. Friction stir post-processing was applied to the EBAM obtained Fe/Cu composite that allowed improving its microhardness and wear resistance [20].

An aluminum bronze/steel composite can be obtained by means of EBAM, where primary solidification of steel grains would eliminate formation of the detrimental columnar bronze ones. Considering the fact that nickel is a highly soluble metal in copper, the bronze will be enriched by drawing nickel from stainless steel and therefore additional intermetallic precipitate may appear that would provide the effect of dispersion hardening. Mechanical strength of the bronze grain structures will improve when primary steel grains solidify and hamper the bronze columnar grain growth.

The objective of this work is to study aluminum bronze/stainless steel composites obtained using EBAM with simultaneous feeding of two dissimilar metal wires.

2 Materials and methods

The stainless steel/aluminum bronze composites (SS/bronze) were prepared using an electron beam wire-feed additive manufacturing machine as shown in Fig. 1. The residual air pressure in the chamber was not higher 5 10^{-5}Pa.

Stainless steel ER321 (Beloretsk Metallurgical Plant "MECHEL", Russia) and CuA19Mn2 bronze (JSC Ural Mining Metallurgical Company, Russia) $\varnothing$1.2 mm wires
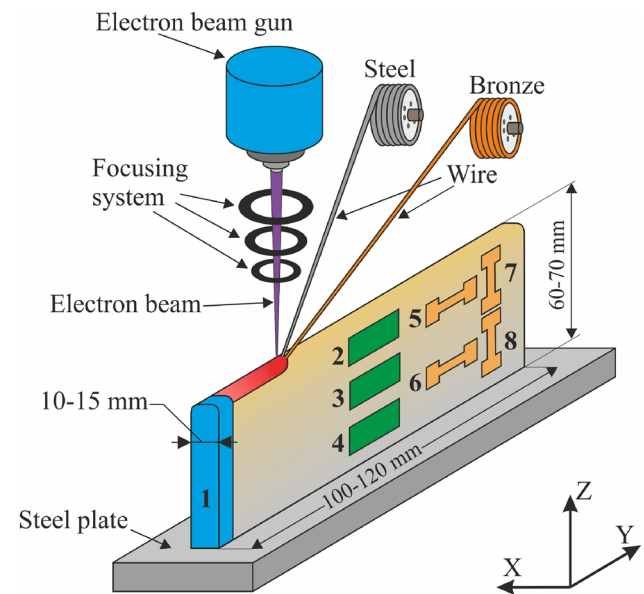
Fig. 1 The scheme of SS/bronze composite wall additive deposition and scheme of cutting off specimens for characterization. 1, 2, 3, 4—samples for microstructural and XRD studies; 5–8 samples for the tensile tests

were continuously fed into a puddle formed in the ER 321 stainless steel substrate by the electron beam, melted there, intermixed in a liquid state and then solidified in the form of an as-deposited layer (Table 1). The very first layers were deposited on the substrate preheated to 350–400 °C and using the electron beam current 74 mA to avoid discontinuities and voids that might form in the substrate/coating transition zone even though the substrate was preheated. The next layers were deposited using the electron beam deposition parameters as follows: $U = 30$ kV, I = 45 mA and using the substrate displacement speed or layer deposition rate 400 mm/min. So the corresponding heat input amounted up to 56.25 J/m.

The desired steel/bronze percentage ratio was supported during deposition by automatic control of the corresponding ratio of the wires' feed rates. Finally, three different composites with the SS/bronze volume fraction ratios 10:90, 25:75, 50:50 were obtained and denoted as follows: 10SS/bronze, 25SS/bronze and 50SS/bronze (see Table 1).

The chemical compositions of the source wires and composites were determined using an X-ray fluorescence (XRF) instrument Niton XL3t 980 GOLDD. On growing the SS/bronze wall the as-deposited metal was characterized for microstructures, phases and mechanical strength using samples EDM cut off the wall as shown in Fig. 1.

Samples for metallographic studies were prepared according to a standard procedure including grinding on the corundum abrasive papers and successively polishing with 14/10, 3/2 and 1/0 grit diamond pastes. On final polishing, the metallographic views were etched by dipping them for a few seconds into the Keller reagent composed of 30 ml $HCl + 5$ g $FeCl_3\text{-}6H_2O + 60$ ml H_2O, followed by washing in distilled water and drying. Macrostructural examination was carried out using an optical microscope Altami Met 1 C. Microstructures and element composition were studied using scanning electron microscope (SEM) Thermo Fisher Scientific Apreo S LoVac attached with an EDS analyzer.

A TEM instrument JEOL-2100 was used for examining the microstructures and phases formed in the composites after solidification. Thin foils for TEM were prepared by EDM cutting $4 \times 2 \times 1$ mm³ platelets from samples 2–4 (Fig. 1) and grinding them to the thicknesses of 0.1 mm.

Then ∅3 mm disks were punched out from them and each of their sides was grinded to make depressions using a Dimpling Grinder Model 200 (Fischione Instruments) machine. The thickness of metal between the two opposite depressions was 10–20 μm. A double ion beam polishing machine TEM Mill Model 1051 (Fischione Instruments) was used at 7 kV ion acceleration voltage for further ion thinning the foil until obtaining a hole with metal edge thickness of 100–200 nm.

An X-ray diffractometer XRD-7000S, Co_{K_α}, and microhardness tester Duramin 5 were used for detecting phases and measuring the microhardness number distribution along the Z axis (Fig. 1) and at 50 g indenter load, respectively.

Uniaxial tensile tests were carried out using a testing machine UTS-110 M on samples 5–8 cut off the wall as shown in Fig. 1. The tensile "dog-bone" samples had the gauge length of 12 mm as well as both thickness and width equal to 2.5 mm. The tensile loading velocity was 1 mm/min.

3 Results and discussion

3.1 Phases and microstructures

The XRD patterns of as-deposited aluminum bronze and SS/bronze composites allow observing the phases formed in them after cooling to room temperatures. The as-deposited bronze is composed mainly of the α-Cu solid solution with moderate amounts of β′-Cu₃Al phase (Fig. 2a) that solidifies directly from the Cu/Al melt in the 8.5–15 wt% Al concentration interval.

The β-phase diagram field shrinks as the temperature is reduced (Fig. 2b) and at 565 °C there occurs a decomposition $\beta \rightarrow \alpha + \gamma_2$, where $(\alpha + \gamma_2)$ is an eutectoid phase [21]. Such a behavior is observed under the equilibrium conditions when cooling is slow and diffusion-controlled redistribution of Cu and Al atoms in the β-phase lattice allows for the eutectoid decomposition. When cooling rate is high enough, no eutectoid decomposition is possible, but, instead, there occurs a diffusionless martensitic transformation of the metastable β-phase into β′, β′₁, and γ′₁-phases (Fig. 2b). It is obvious that all these phases contain the same

**Table 1** Chemical compositions of wires and SS/bronze composites

Material	Elements, wt%									
	C	Cr	Ni	Mn	Ti	Si	Fe	Cu	Al	Zn
ER321	0.06 ± 0.02	17.8 ± 0.09	9.9 ± 0.2	1.1 ± 0.7	0.8 ± 0.03	0.3 ± 0.01	bal.	–		–
CuA19Mn2	–	–	–	1.9 ± 0.04	–	–	0.3 ± 0.01	bal.	9.3 ± 1.4	0.4 ± 0.02
10SS/bronze	–	2.2 ± 0.04	1.3 ± 0.03	1.4 ± 0.03	0.05 ± 0.008	0.05 ± 0.02	7.7 ± 0.05	80.7 ± 0.6	6.2 ± 0.04	0.2 ± 0.02
25SS/bronze	–	5.7 ± 0.05	2.9 ± 0.05	1.1 ± 0.04	0.1 ± 0.01	0.1 ± 0.05	19.1 ± 0.08	65.3 ± 0.5	5.33 ± 0.5	0.1 ± 0.01
50SS/bronze	–	9.9 ± 0.05	4.6 ± 0.06	1.09 ± 0.04	0.2 ± 00.1	0.2 ± 0.06	33.8 ± 0.1	46.2 ± 0.4	3.7 ± 0.5	0.05 ± 0.02
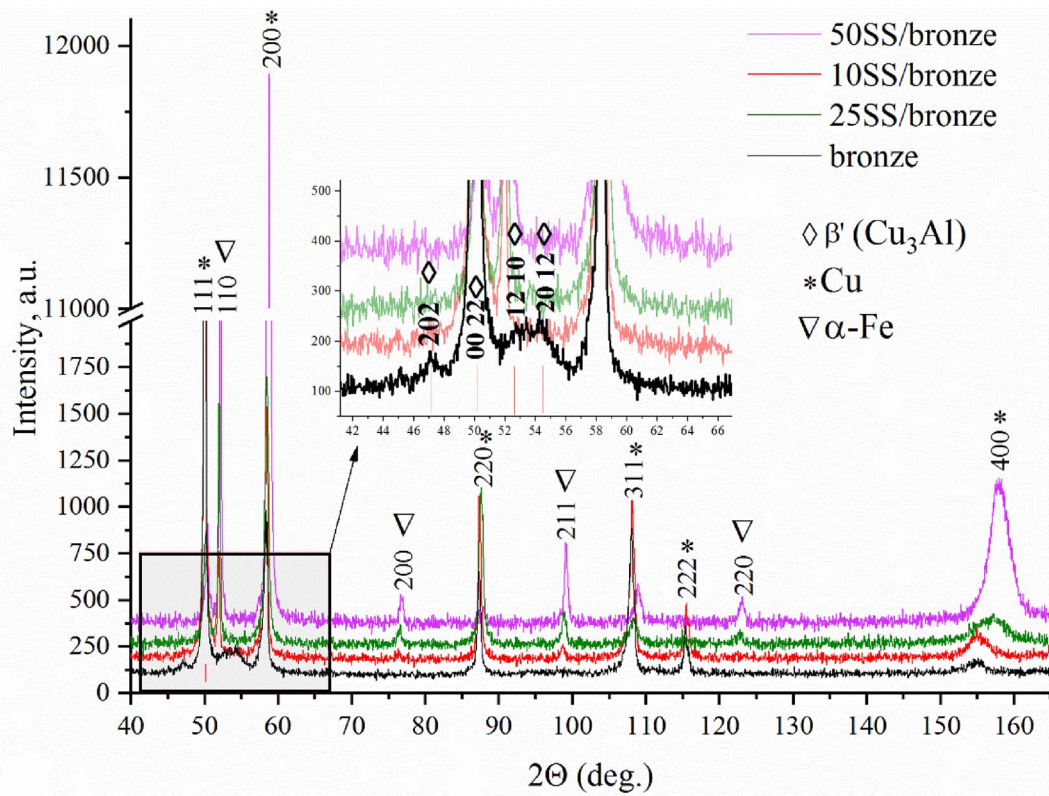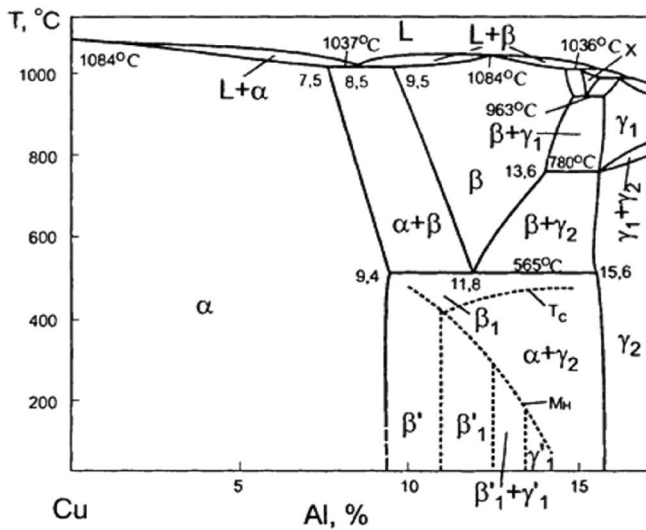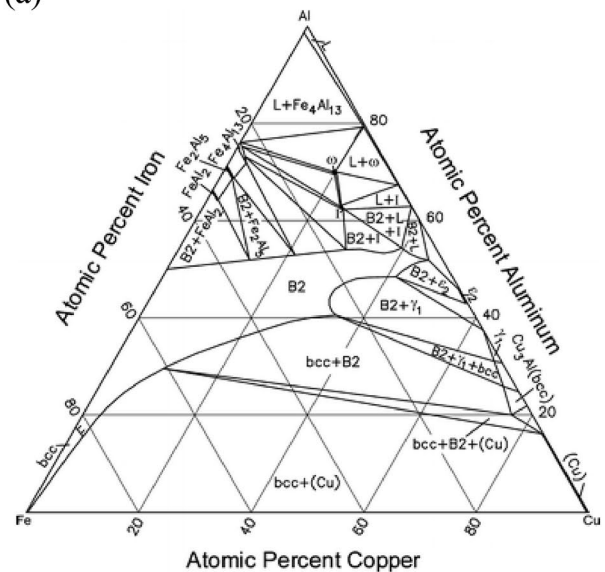
Fig. 2 The XRD patterns of as-deposited bronze and SS/bronze composites (**a**), Al–Cu (**b**) [21] and Cu–Al–Fe (**c**) [23] diagrams

concentrations of elements as the parent one and differ only by their crystalline lattices.

The martensitic β′-phase is an inherently disordered phase formed directly from the disordered parent β-phase (β → β′) (Fig. 2b) while other ones are such as β′$_1$ and γ′$_1$ are the inherently ordered ones as those stemming from the ordered β$_1$ phase according to reactions: β$_1$ → β′$_1$ and γ$_1$ → γ′$_1$. Here and below, the suffix number "1" will refer to the ordered phases. It seems that the cooling rate was high enough to enable martensitic transformation of

β′-Cu$_3$Al in the electron beam wire-feed additive deposited metal.

The XRD patterns of the SS/bronze composites revealed the presence of α-Fe whose contents grow with that of the SS intermixed with the bronze (Fig. 2a). The α-Cu peaks are shifted to the low 2Θ end as compared to those of standard Cu ones because of possible nickel dissolution in the α-Cu [14, 22]. In fact, these aluminum bronze grains became the nickel aluminum bronze ones and therefore will be denoted below as α-Cu(Al, Ni). No presence of the β′-phase was detected in SS/bronze composite samples (Fig. 2a).

Macrostructural optical views are shown in Fig. 3 that allow observing structures formed in the as-deposited SS/bronze composites. Transition ∼ 2–3 mm of thickness zones were formed in the vicinity of the stainless steel substrates in all composites due to intermixing and dilution of the transferred metals in a partially melted substrate (Fig. 3a, f, k). These transition zones formed in the 10SS/bronze and 25SS/bronze composites (Fig. 3b and g) are characterized by sharp defectless fusion boundaries as well as coarse bronze regions inside the steel matrices while that of 50SS/bronze composite is distinguished by its fine steel grains with the grain boundary bronze structures (Fig. 3l). The microstructures found in both medium and top parts of the 10SS/bronze and 25SS/bronze composites show fine globular particles in the bronze matrix (Fig. 3d, h) together with some larger ones (Fig. 3c, i). The 50SS/bronze composite reveals its more homogeneous structure with the steel dendritic structures as well as coarse steel particles located in the bottom part of the wall (Fig. 3m, n). A thin dark-etched α-Fe transition zone can be seen between the large bright non-etched γ-Fe grain and bronze matrix in Fig. 3m. It seems that solidified stainless steel drops were partially transformed into α-iron during cooling. The mechanism responsible for such a γ → α transformation may be redistribution of nickel in favor of the aluminum bronze. The top part structures of all the composites demonstrate isolated steel particles (Fig. 3e, j, o).

It is worthwhile to note that the transition zone is free from defects such as pores, cracks or discontinuities despite their presence being reported elsewhere [2, 15]. The reason behind such a finding is using the higher heat input when depositing the first several layers.

3.1.1 Microstructures in 10SS/bronze

The detailed SEM examination of structures formed in the 10SS/bronze composites showed the presence of residual lamellar particles in the bronze matrix near the steel grains (Fig. 4a, b). The corresponding SAED pattern and dark-field images obtained from this particle using the ($\overline{1}01\overline{2}$) reflection allow identifying these particles as those belonging to the β′-phase (Fig. 4c, d). The dark-field image in Fig. 4e was obtained also using an α-Cu(Al,Ni) reflection to observe the

matrix contrast. An EDS analysis of corresponding areas shows them as containing ∼ 21 at.% Al and ∼ 73 at.% Cu, i.e., of concentration ratio corresponding to that of Cu$_3$Al (Fig. 4c, Table 2, spectra 1 and 2).

The globular 0.8 ± 0.02 μm in size particles can be distinguished in the 10SS/bronze composite's matrix (Fig. 4f) that were identified as the α-Fe(Cr) solid solution according to the dark-field image (Fig. 4g) and EDS spectra 3–5 (Table 2) obtained from particles numbered in Fig. 4f. The fine faced 48 ± 1.4 nm precipitates can be seen inside the α-Fe(Cr) (Fig. 4h) that were identified as copper-rich ones. These particles precipitated from the solidified α-Fe(Cr) grains during cooling and can be coherent with the α-Fe(Cr) matrix (Fig. 4h).

Another sort of fine and faced ∼ 80 nm in size precipitates may be observed in the α-Cu(Al,Ni) matrix together with the dislocation loops formed due to coalescence of diffusion vacancies (Fig. 4i, g). The SAED pattern (Fig. 4i), EDS analysis of areas 7 and 8 in Fig. 4g (Table 2) and dark-field TEM image obtained using the ($2\overline{2}0$) reflection (Fig. 4k) allowed identifying them as D03 AlFe$_3$ or κ$_{iv}$-phase. The presence of bend extinction contours around these particles (Fig. 4i, g) can be related to microstresses generated on the particle/matrix boundaries due to partial crystalline lattice incompatibility. These stresses may sufficiently increase the α-Cu(Al,Ni) strength.

3.1.2 Microstructures in 25SS/bronze

Large α-Fe(Cr) particles were found in the 25SS/bronze composite with their mean size equal to 12.58 ± 0.37 μm (Fig. 5a, b). These particles were the first ones to solidify from the melt as γ-Fe(Ni,Cr) dendrites and then would be transformed to α-Fe(Cr) by the loss of nickel in favor of α-Cu. (Table 2, spectra 3–5). It is also known [2, 24] that some amount of δ-ferrite can be solidified directly from the melt in the as-deposited Cu–Al–Fe and aluminum bronze coatings. Therefore, it is not unthinkable that some α-Fe(Cr) grains could directly solidify along with the γ-Fe(Ni,Cr) ones. The large α-Fe(Cr) grains contain some submicron-(Fig. 5b) and nano-sized (Fig. 4h) Cu-enriched precipitates. It is suggested that these particles precipitated from already solidified α-Fe(Cr) grains during their cooling to room temperatures and corresponding reduction of residual copper content in iron to zero.

The TEM images enabled observation of even finer globular and rod-like particles inside the α-Fe(Cr) grains (Fig. 6a, d). Corresponding EDS maps show that these rod-like particles contain more copper (Fig. 6i, spectra 3–4, Table 3) as compared to that of globular ones (Fig. 6i, spectra 1–2, Table 3). These 0.33 ± 0.01 rod-like precipitates were identified as β′-phase according to their SAED pattern and dark-field image examination (Fig. 7a, b, c, d). These
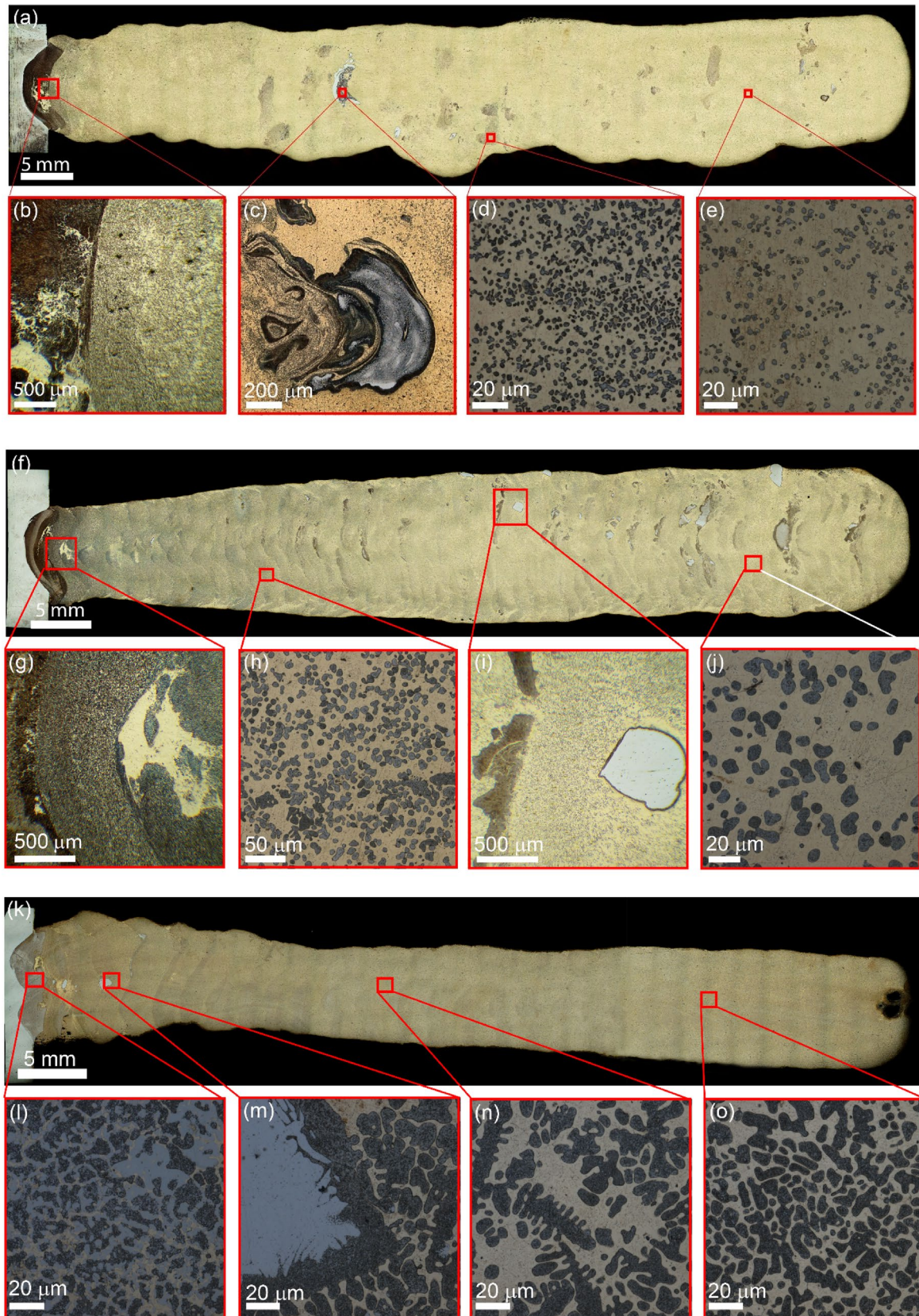
**Fig. 3** Macro and microstructures of 10SS/bronze" (**a–e**), "25SS/bronze" (**f–j**) and 50SS/bronze composites (**k–o**)
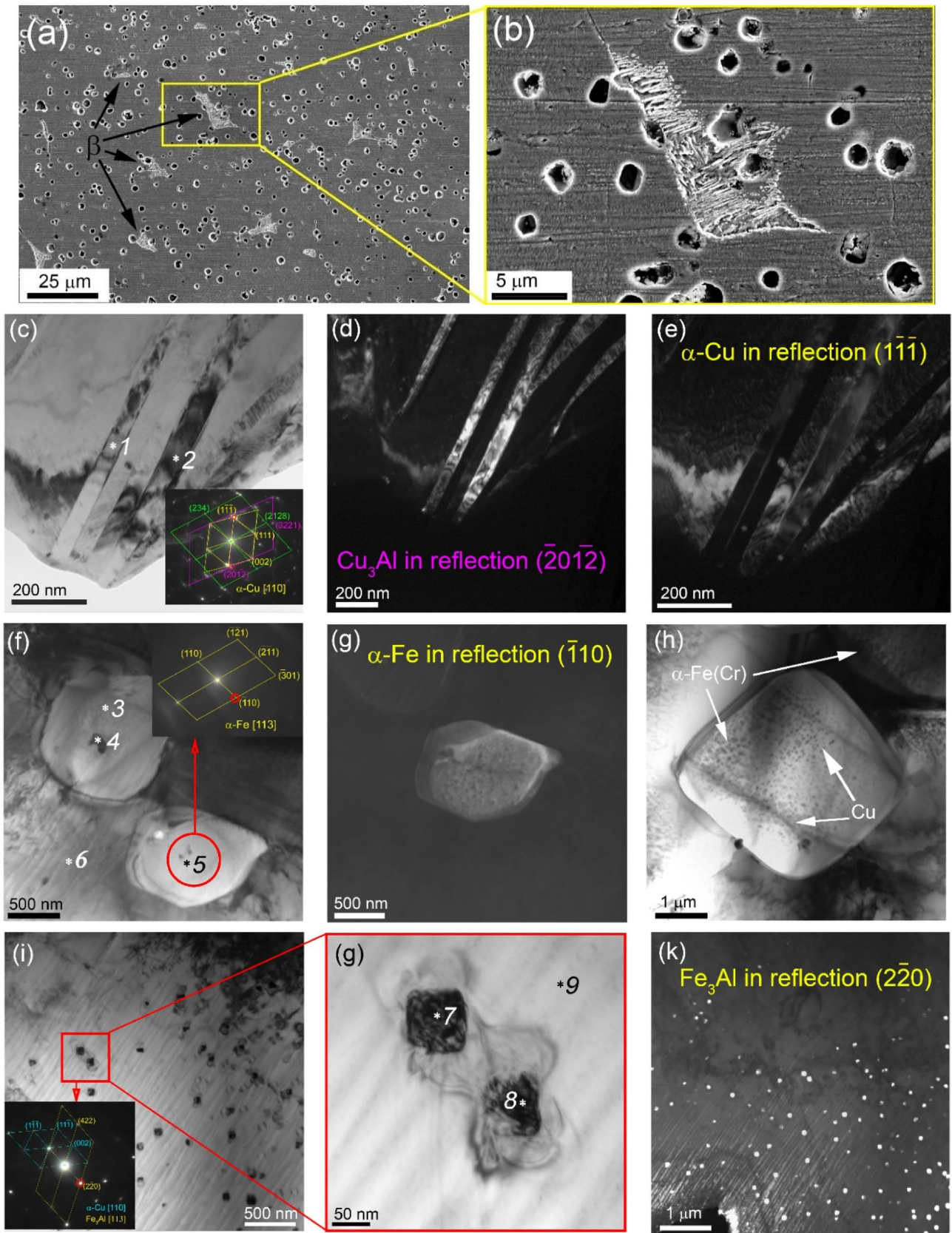
Fig. 4 SEM BSE images (**a**, **b**), TEM bright-field (**c**, **f**, **h–g**) and dark-field (**d**, **e**, **j**, **k**) images of microstructures of as-deposited 10SS/bronze composite. 1–9—denote points selected for EDS (Table 2)

Table 2 EDS analysis of the 10SS/bronze composite obtained using TEM (Fig. 4c, f, g)

Spectrum	Chemical composition, at.%								Structure
	Al	Si	Cr	Mn	Fe	Co	Ni	Cu	
Spectrum 1	21.11	0.91	0.10	1.64	0.55	0.09	2.00	73.59	Cu_3Al
Spectrum 2	21.65	0.62	0.23	1.96	0.37	0.10	2.11	72.97	Cu_3Al
Spectrum 3	6.46	1.54	22.88	2.36	60.79	0.22	0.54	5.22	α-Fe(Cr)
Spectrum 4	6.30	1.80	22.93	2.16	59.97	0.28	0.58	5.98	α-Fe(Cr)
Spectrum 5	7.49	1.71	22.17	2.51	59.05	0.26	0.56	6.25	α-Fe(Cr)
Spectrum 6	7.46	0.19	0.34	1.62	2.58	0.11	1.05	86.65	α-Cu
Spectrum 7	12.58	1.36	5.05	2.32	33.16	1.06	0.88	43.58	Fe_3Al
Spectrum 8	14.97	0.79	1.65	1.71	13.08	1.36	1.17	65.26	Fe_3Al
Spectrum 9	15.05	1.36	0.32	1.27	1.96	1.01	1.15	77.88	α-Cu

Fig. 5 SEM SE (**a**) and BSE (**b**) image of microstructures in 25SS/bronze composite
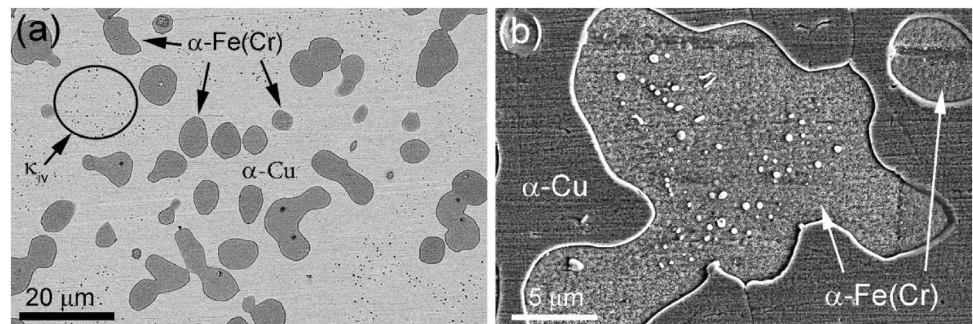
β′-phase precipitates allow observing their inner martensitic type microstructure in Fig. 7b, d.

Globular 0.26 ± 0.01 μm in size precipitates (Fig. 6d, pos.1 and 2) were found in the α-Fe(Cr) grain center while even finer 68 ± 2 nm ones were located closer to the α-Fe(Cr) grain boundary.

It should be noted that comparing the EDS profiles of Al and Ni obtained along the yellow line in Fig. 7a with that of Cu (Fig. 7i), it may be suggested that the β′-phase precipitates boundaries in Fig. 7i are enriched with Al (~ 7 at.%) and Ni (~ 15 at.%) so that this precipitate may be a core/shell particle with the Cu_3Al core and AlNi shell. The mean size of the $κ_{iv}$-phase precipitates in the α-Cu(Al, Ni) grains is 115 ± 3.3 nm, i.e., by a factor of 1.5 larger than that of the 10SS/bronze (Fig. 5b).

3.1.3 Microstructures in 50SS/bronze

Instead of isolated α-Fe(Cr) grains, the 50SS/bronze composite demonstrates dendritic steel structures in the α-Cu(Al,Ni) matrix (Fig. 8a, b). These α-Fe(Cr) dendrites additionally contain fine globular and rod-like precipitates (Fig. 8b–e) the same as those discussed above and found in the 25SS/bronze composite.

By analogy with the TEM results obtained on the 25SS/bronze, these rod-like precipitates inside the α-Fe(Cr)

grain (Fig. 8c) can be the β′-phase ones inside the AlNi shells. Along with that, coarse β′-grains are also observable in these grains (Fig. 8d, c) whereas the α-Cu(Al,Ni) grains contain 150 nm in size $κ_{iv}$-phase precipitates.

The TEM images in Fig. 9a, b may lend support to the suggested above formation of the core/shell β′/AlNi precipitates. The SAED pattern in Fig. 9c allows identifying the AlNi crystalline lattice. The dark-field images in Fig. 9d, e, f were obtained using reflections $(0\bar{1}0)_{AlNi}$, $(2118)_{β'}$ and $(\bar{1}10)_{α-Fe}$, respectively, and serve for reliable identification of the precipitates by their contrast. It can be observed also from a comparison between Fig. 9d and Fig. 9e that the $(0\bar{1}0)_{AlNi}$ reflection allows exposing rectangular shells around the β′-phase precipitates. Let us note again that many β′-precipitates in Fig. 9d cannot be observed in Fig. 9e because of full shielding by their AlNi shells. The mean size of the β′/AlNi precipitates is 0.32 ± 0.03 μm.

Globular 0.32 ± 0.01 μm Cu-enriched particles are located in the central part of the α-Fe(Cr) grains with the AlNi shells around them (Fig. 10a, b). The smaller 37 ± 1.1 nm ones can be found in the vicinity of the α-Fe(Cr) boundaries (Fig. 8c, e). It can be noted that the EDS profiles show the presence of Al and Ni peaks on both Cu peak sides (Fig. 10b) meaning that there is an AlNi shell around this Cu-Al-Ni particle.
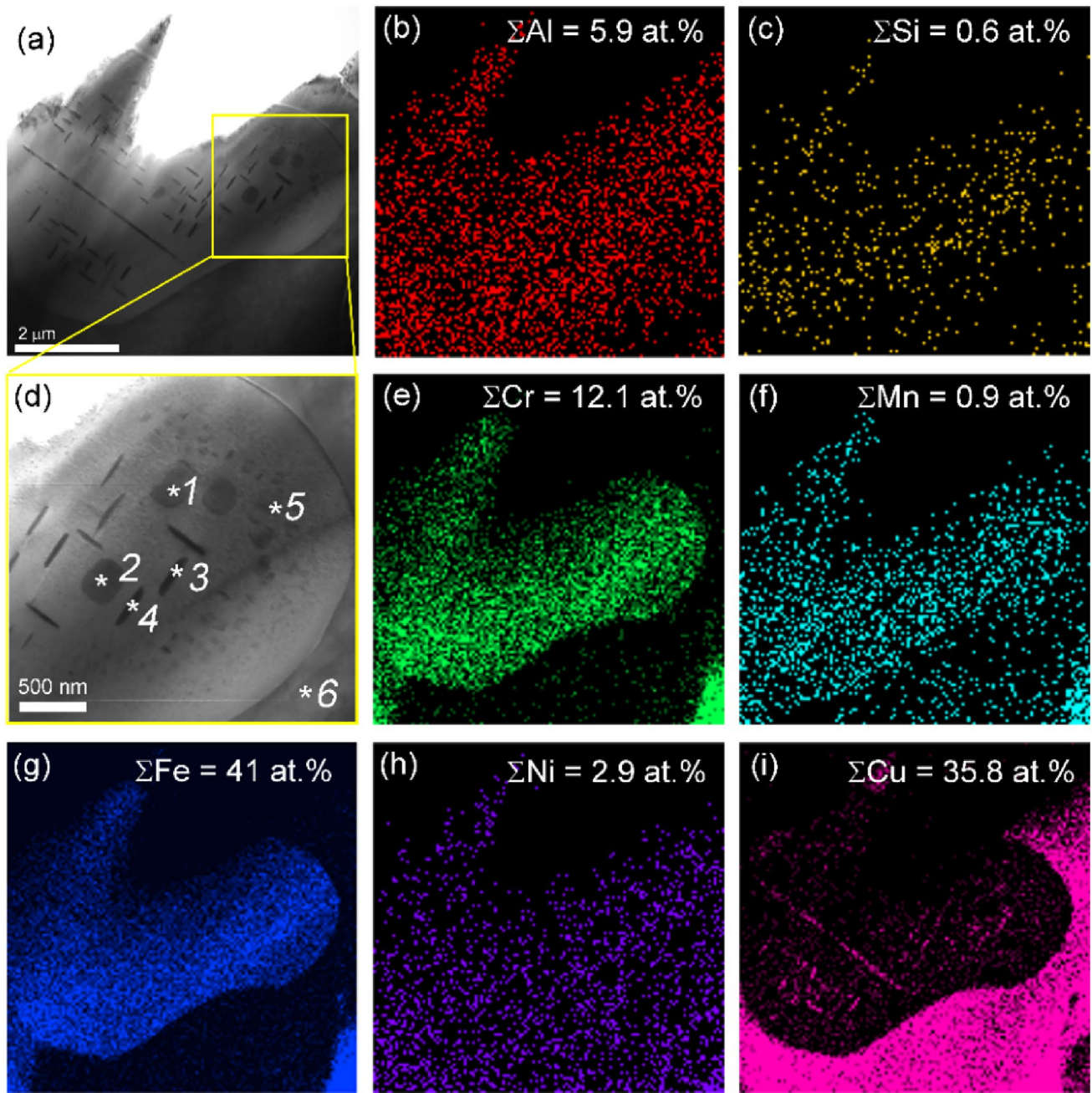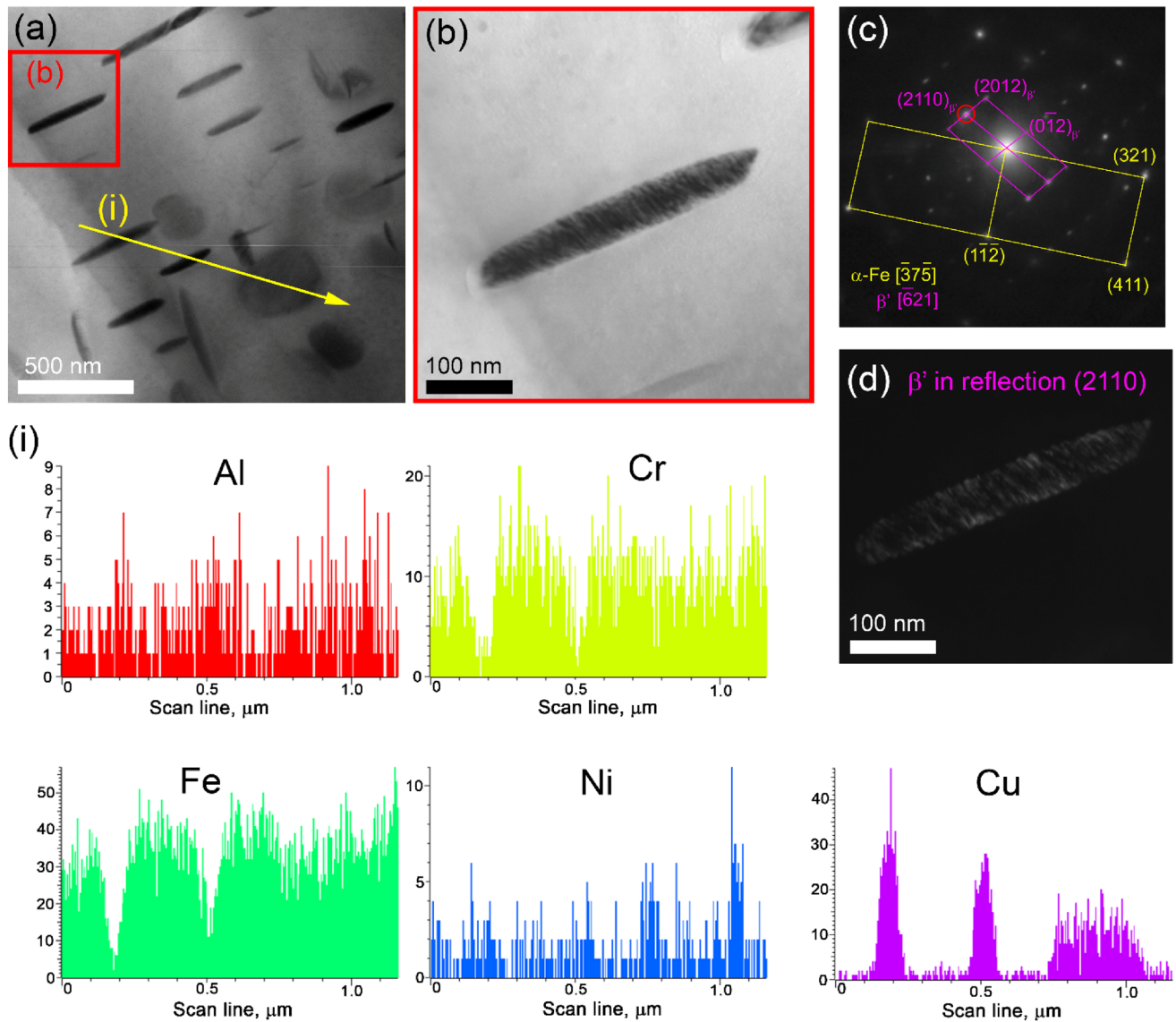
Fig. 6 Bright-field TEM images of precipitates inside the α-Fe(Cr) grain of 25SS/bronze composite (**a**, **d**) and corresponding EDS element distribution maps (**b**, **c**, **e–i**)

Table 3 EDS analysis of the 25SS/bronze composite (see particles numbered in Fig. 6d)

Spectrum	Chemical composition, at.%						
	Al	Si	Cr	Mn	Fe	Ni	Cu
Spectrum 1	6.14	1.57	17.58	1.02	57.21	2.67	13.81
Spectrum 2	7.97	1.87	15.85	1.06	52.80	2.57	17.87
Spectrum 3	9.16	1.15	10.92	0.88	35.02	3.25	39.62
Spectrum 4	9.12	1.38	5.73	0.93	19.40	3.05	60.40
Spectrum 5	6.63	2.63	19.36	1.07	64.98	1.86	3.48
Spectrum 6	7.23	–	0.72	1.09	4.52	3.64	82.80

Fig. 7 The bright-field TEM image of α-Fe(Cr) grain in the 25SS/bronze composite (**a**), enlarged view of the core/shell β′/AlNi precipitate (**b**), SAED pattern (**c**); dark-field image obtained using $(2110)_{β'}$ reflection (d), EDS spectra (i) along the yellow line in **a**

3.1.4 Microhardness and tensile strength

The microhardness numbers are used for characterizing mechanical characteristics of small volumes in distinction to the integral characteristics obtained from a tensile test. The corresponding microhardness profiles were obtained for as-deposited bronze and SS/bronze composites as measured along the wall height and starting from the substrate (Fig. 11). All these microhardness profiles clearly show the presence of a transition zone where the substrate metal was intermixed with the metal transferred from the wires. The hardness of this zone is determined by the amount of steel intermixed with bronze.

The as-deposited SS/bronze composites demonstrate their microhardness numbers that depend on the amount of steel in the composite, i.e., the as-deposited 50SS/bronze, 25SS/bronze and 10SS/bronze composites demonstrate maximum, medium and minimal microhardness levels, respectively. Let us note that the microhardness number distributions in Fig. 11 represent the characteristics of both components, i.e., relate to both steel and bronze grains.

The microhardness of the as-deposited aluminum bronze is at the level of 1.4 GPa with some 2 GPa peaks resulted from indenting the Cu_3Al precipitates (Fig. 11). This is close to that of the 10SS/bronze composite. Sufficiently higher bronze matrix microhardness numbers were obtained on
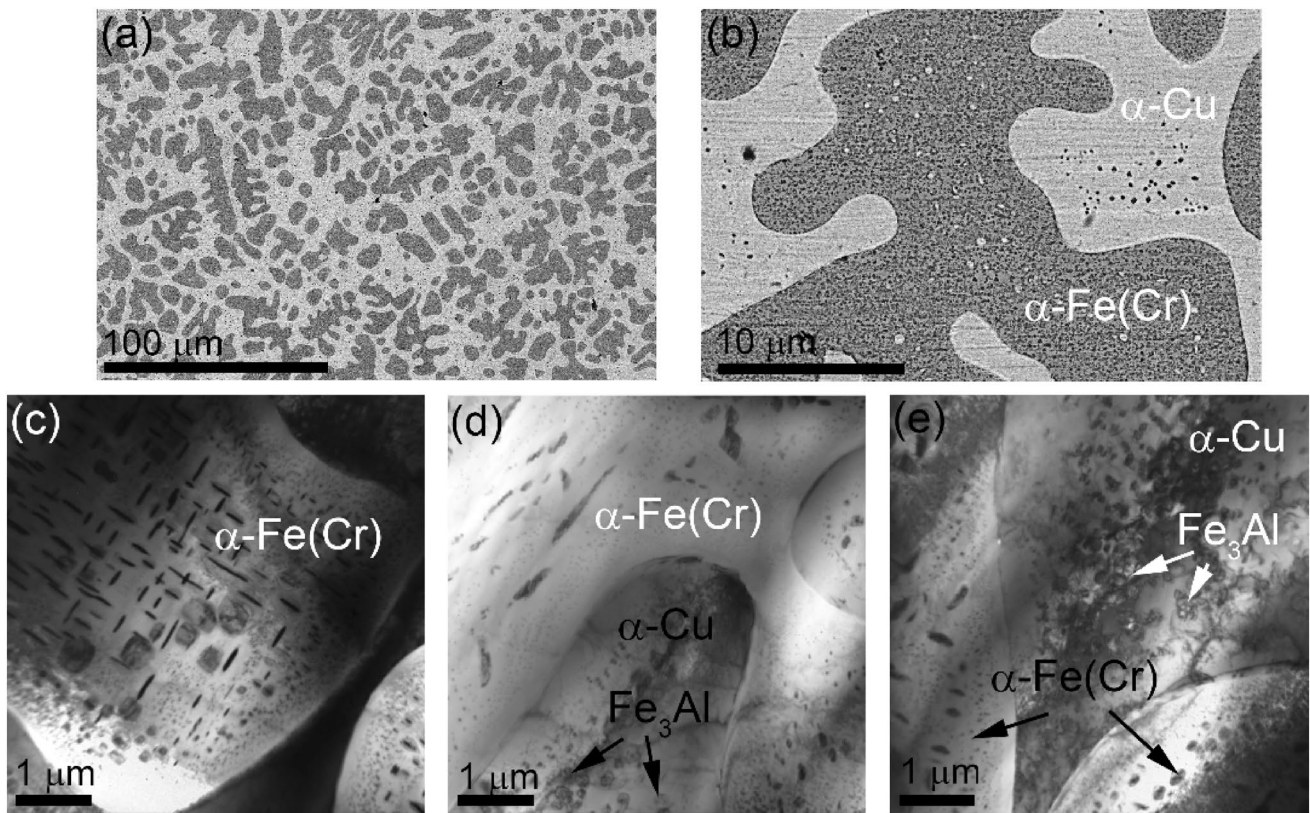
Fig. 8 SEM SE images of steel dendrites (**a**) and coarse globular particles in α-Cu(Al,Ni) and α-Fe(Cr) grains (**b**) in the 50SS/bronze composite. TEM bright-field image of precipitates in α-Fe(Cr) (**c–e**) and α-Cu(Al,Ni) grains (**d, e**)

25SS/bronze and 50/SS bronze composites. Therefore, it may be stated that the bronze matrix grains were dispersion hardened as compared to those in the as-deposited bronze and 10SS/bronze ones. The same is true for the α-Fe(Cr) grains as compared to those in the 10SS/bronze.

The tensile strength tests showed a notable anisotropy of mechanical characteristics obtained on the as-deposited bronze samples (Fig. 12) that depended on the tensile axis orientation with respect to the coordinate system in Fig. 1. On the other hand, these differences are less manifested on the strain/stress curves of SS/bronze composites, i.e., their composite structure has a good effect on the uniformity of mechanical characteristics. All the composites demonstrated the tensile strength increasing with the content of steel in them as well as simultaneously decreasing the strain-to-fracture values. For instance, the 50SS/bronze composite demonstrated the maximum ~ 800 MPa ultimate tensile stress and minimum 0.18% strain-to-fracture as compared to those of 10SS/bronze and 25SS/bronze.

The most notable improvement of strength without a great loss in plasticity can be observed for the 10SS/bronze sample that may be related to effective dispersion hardening of the α-Cu(Al,Ni) grains by κ_{iv}-phase precipitates. Let us remember that the mean size of the κ_{iv}-phase precipitates

changed from 80 nm in 10SS/bronze to 115 nm in 25SS/bronze and finally to 150 nm in 50SS/bronze samples.

The strengthening rate $d\sigma/d\varepsilon$ curves do not show any features that could have been recognized as a twinning stage (Fig. 12b). It seems that dislocation gliding was the main deformation mechanism in the α-Cu(Al,Ni) grains.

Fracture surfaces of all samples reveal viscous intergranular type of fracture with numerous ridges (Fig. 13). The EDS Fe distribution maps were superimposed on the SEM fractography images to identify the α-Fe(Cr) grains and even dendrites (Fig. 13c). The finest and scarce α-Fe(Cr) grains were observed on the fracture surface of the SS10/bronze composite (Fig. 13a), the larger ones are in the SS25/bronze (Fig. 13b), and the maximum ones are in the SS50/bronze (Fig. 13c). Since there is not much difference in hardness between the α-Cu(Al, Ni) and α-Fe(Cr) grains (Fig. 11) inside the same composite, one can suggest that all these grains experience plastic deformation during loading. At the same time, the SS50/bronze contains more nickel and iron so that its grains are more dispersion hardened as compared to those of the SS25/bronze and especially of the SS10/bronze ones. Therefore, some large flat areas can be found in Fig. 3c that may be related to those of α-Fe(Cr) grains reinforced with the core/shell precipitates (Fig. 4g). It seems that the
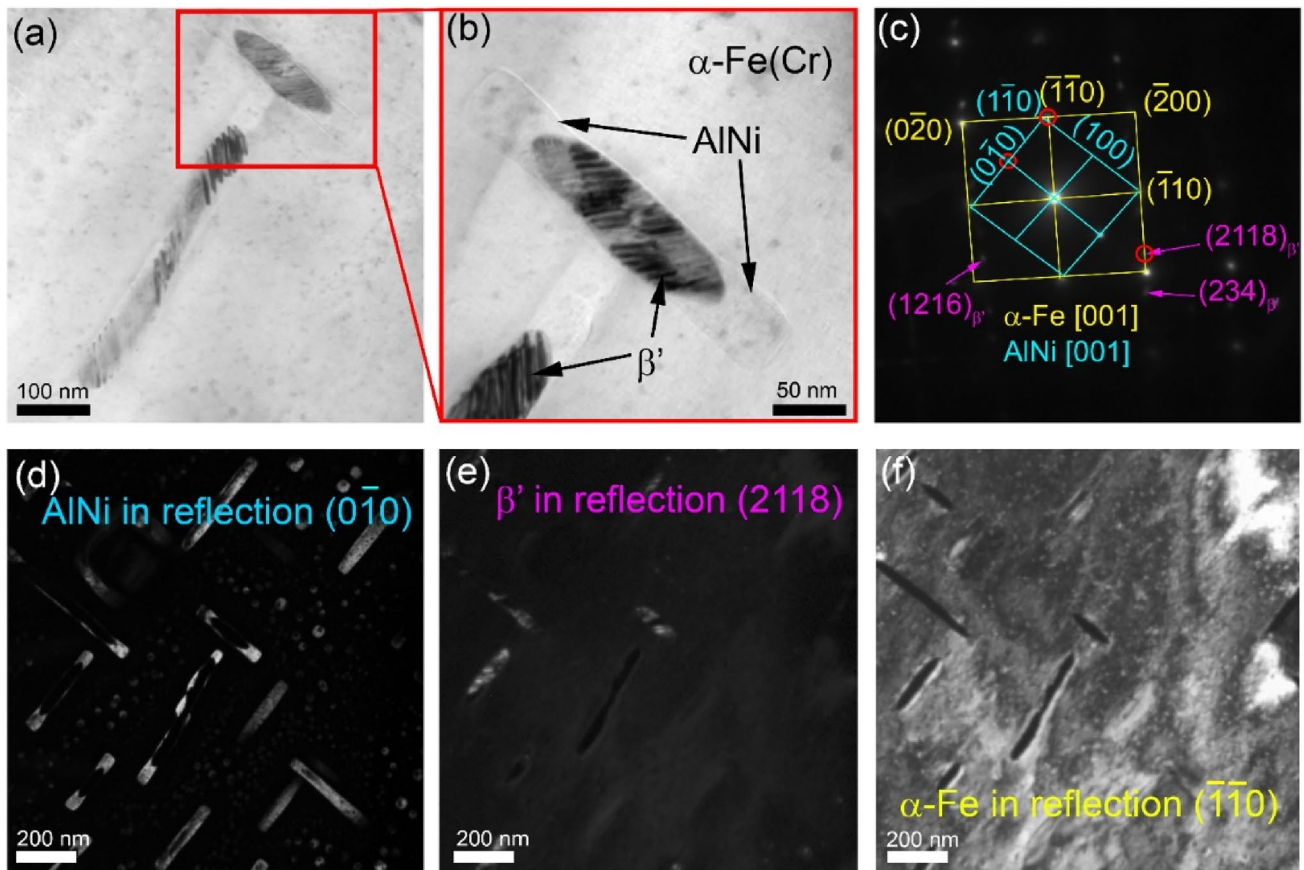
Fig. 9 Bright-field TEM images of β′/AlNi precipitates (**a**, **b**), SAED pattern (**c**) and dark-field TEM images of AlNi shells, β′-cores and α-Fe(Cr) matrix obtained using reflections $(0\bar{1}0)_{AlNi}$, $(2118)_{β'}$ and $(\bar{1}10)_{α-Fe}$, respectively

excess of these particles in α-Fe(Cr) grains of SS50/bronze sample resulted in their brittle-like transgranular fracture.

The TEM images were obtained from thin foils cut off the tensile specimens in the vicinity of the fracture surfaces, where the maximum strain was achieved (Fig. 14). The deformed zone structures allow identifying the presence of thin and fine deformation microtwins (Fig. 14a, c, d) as well as dislocation structures in the bronze grains. The ferrite grains were reinforced by precipitates and therefore were almost free of dislocations as well as retained their undistorted shapes (Fig. 14b, d, f). These results lend support to the suggestion that deformation was developing mainly by the bronze grains and mostly according to the dislocation gliding mechanism with only small twinned areas.

4 Discussion

4.1 Microstructures and precipitations

The basic chemical elements of the alloys intermixed in a melted pool were immiscible iron and copper, while the

other ones were miscible aluminum, nickel and chromium. It was shown earlier [17] when studying the additive manufacturing of a stainless steel/copper composite that only copper and stainless steel grains were formed, i.e., no copper/nickel solution was observed. The stainless steel dendrites were first to solidify from the melt while copper solidified later in the interdendrite spaces. This is how primary dendritic structures were formed in EBAM. However, some amounts of copper and iron were dissolved in each other below the corresponding solidus temperatures. When cooling these metals were forced out of the corresponding lattices and precipitated in the form of fine particles. Also no δ-ferrite was detected in the stainless steel regions despite it being often found in the as-weld stainless steel structures [17].

Another finding was that the γ → α transformation occurred in a manner that almost all stainless steel grains have been transformed into ferrite ones except for the huge ones with a stainless steel core enveloped by the ferrite shell. Such a finding suggests that solidification of the SS/bronze melted pool started from nucleation and growth of γ-grains or dendrites depending on the stainless steel percentage transferred to the melted pool.
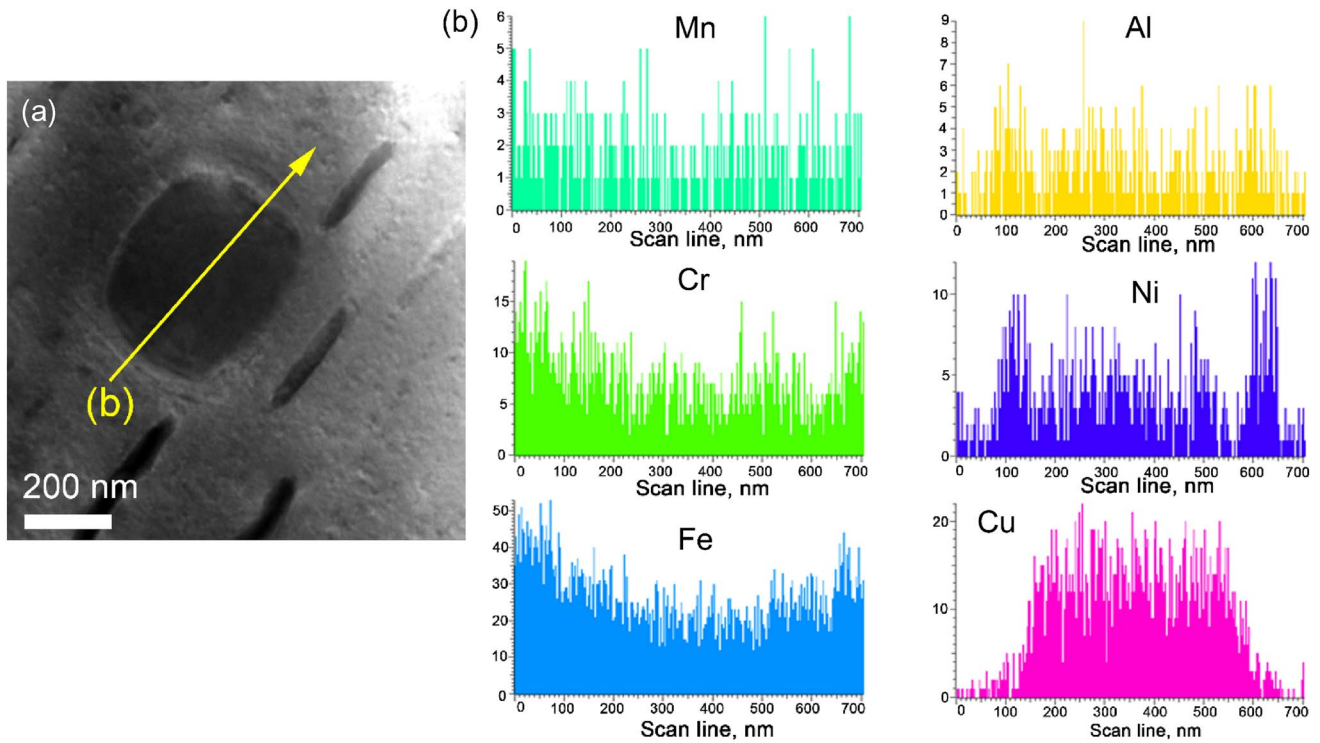
Fig. 10 Bright-field TEM image of globular copper-rich particle (**a**) with corresponding EDS linear spectra (**b**)
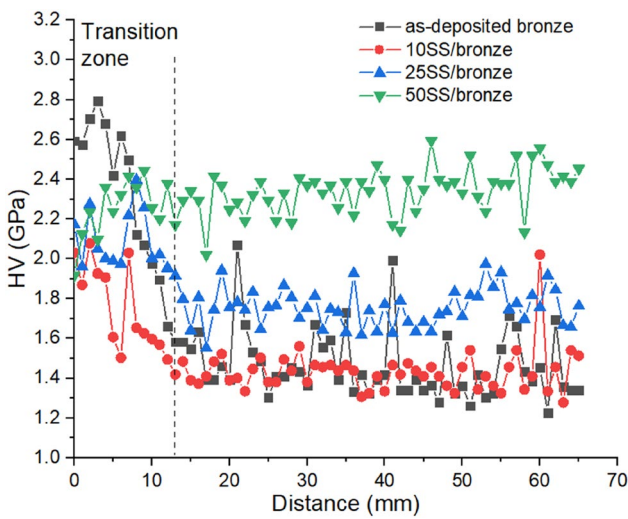

Fig. 11 Microhardness profiles for as-deposited bronze and SS/bronze composites

It is not inconceivable at this stage that some amount of δ-ferrite solidified too according to reaction L → γ + δ [25] but chances are that the FCC copper is an austenite-promoting element and therefore might interfere with the ferrite solidification from the copper–rich interdendrite spaces. The intensive intermixing between liquid SS and bronze might cause dissolution of both components in each other so that

the SS regions will be enriched with copper and aluminum while bronze dissolves some iron and as much as possible of nickel. The depletion by nickel may reduce the nickel equivalent and change the stainless steel droplet's solidification mode from AF to FA [25], where A and F are the austenite and ferrite, respectively. The latter is especially important for the small stainless steel droplets solidifying inside the liquid bronze environment. Comparing chemical compositions of the ER321 wire (Table 1) and small ferrite grains (recalculated into weight percentages from Tables 2 and 3) one can see that concentration of nickel in the latter reduced greatly, in fact, from 9.9 wt% to about 1÷0.6 wt%. As can be observed from the pseudobinary section of the Fe–Cr–Ni diagram at 70 wt% Fe [25] that such a depletion corresponds to the FA solidification mode.

Another situation is with the large SS drops that solidify as primary SS grains or dendrites while their peripheral regions lose nickel and transform into ferrite.

The interchanging diffusion processes still continue even after full solidification of the composite. The solvability of copper in α-iron becomes close to zero with cooling so that small globular copper/aluminum particles precipitate there and this interchanging diffusion starts again between solid copper/aluminum particles and iron/nickel environment. As a result, these copper/aluminum particles become covered by the AlNi shells. It is worth noting that the enthalpy of AlNi formation is ΔH = − 127 kJ/mol, i.e. lower than
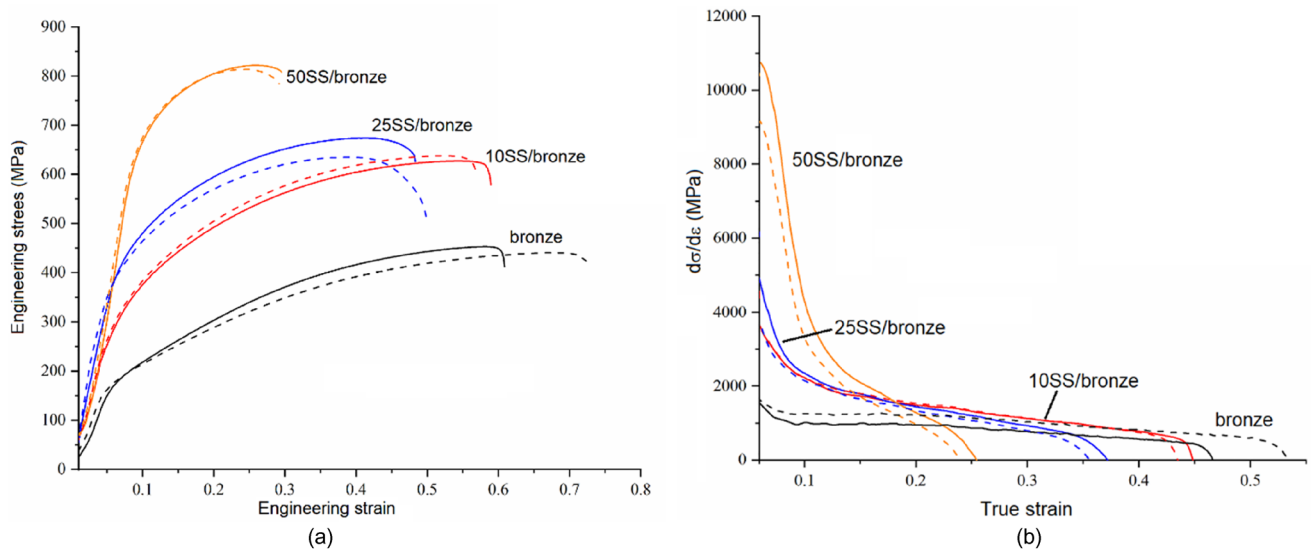
Fig. 12 Stress–strain (**a**) and strengthening rate (**b**) typical curves obtained on as-deposited samples of as-deposited aluminum bronze and SS/bronze composites. Solid and dash lines denote tensile curves obtained from samples 5–6 and 7–8 (Fig. 1), respectively
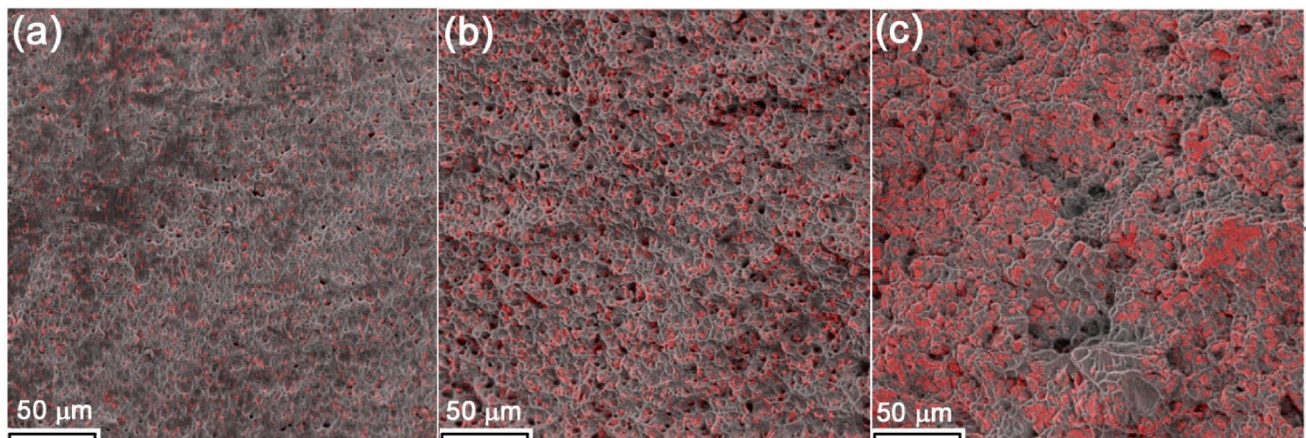
Fig. 13 Tensile test fracture surfaces on samples SS10/bronze (**a**), SS25/bronze (**b**) and SS50/bronze (**c**). Red color shows distribution of α-iron obtained from the EDS

$\Delta H = -73$ kJ/mol of the Cu_3Al β'-phase. This is how the core/shell β'/AlNi precipitates appear in the steel grains. According to [26] a miscibility gap between Cu_3Ni and AlNi phases may really exist.

The bronze grains thus contain dissolved iron and nickel in addition to residual aluminum. Therefore, in cooling to 700 °C, the $AlFe_3$ κ_{iv}-phase may precipitate there. The enthalpy of the κ_{iv}-phase formation is $\Delta H = -77$ kJ/mol and therefore its precipitation is a bit more preferable as compared to that of Cu_3Al β'-phase with $\Delta H = -73$ kJ/mol.

It is interesting that both 25SS/bronze and 50SS/bronze composites do not reveal any coarse β'-grains as those found in the as-deposited bronze and 10SS/bronze composite. The suggestion is that α-Cu(Al,Ni) solid solution becomes

depleted by aluminum which could be in need for the $AlFe_3$ precipitation.

4.2 Deformation

Mechanical characteristics of the SS/bronze composites strongly depend on the content of the stainless steel intermixed with the bronze and, therefore, the highest ultimate tensile strength was achieved on the 50SS/bronze composite. The double wire feed provided intensive intermixing of the components and created a relatively homogeneous distribution of them over the wall's volume with effective strengthening of the entire structure. Let us dwell on some specifics of such a composite in terms of deformation.
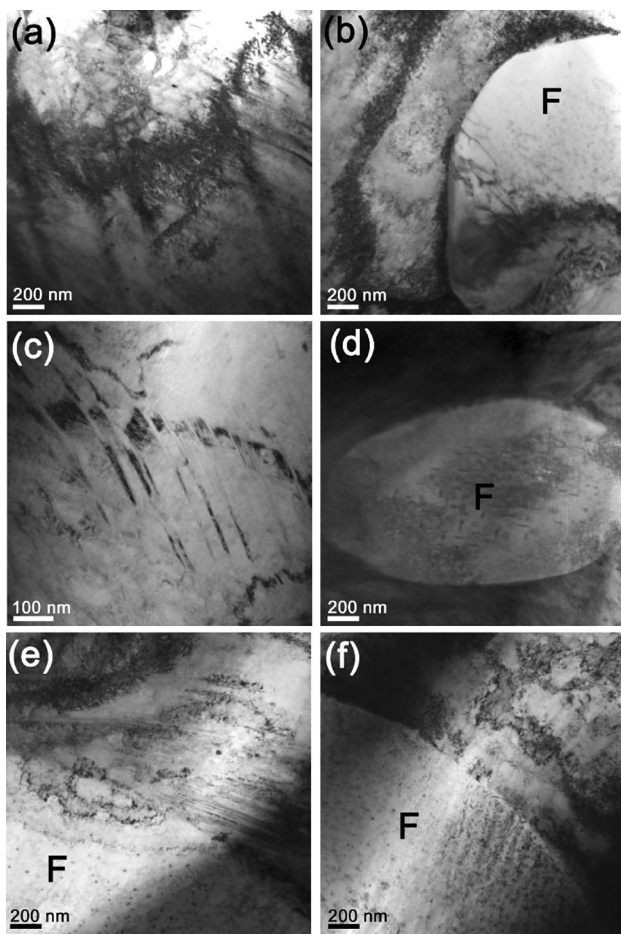
Fig. 14 Deformation twins (**a**, **c**, **e**) in the α-Cu(Al,Ni) grains and ferrite(F)/bronze boundaries (**b**, **d**, **f**) of SS10/bronze (**a**, **b**) SS25/bronze(**c**, **d**) and SS50/bronze (**e**, **f**) samples. F stands for ferrite

The plastic deformation in the BCC ferrite is by dislocation mechanisms while copper/aluminum bronze is also capable of twinning. It is obvious that the composite's bronze matrix has its yield stress lower than that of the ferritic grains and therefore all deformation changes will be concentrated in the bronze matrix. The steel grains or dendrites serve as reinforcement of the matrix and would then carry mainly elastic stresses.

Structural changes in the α-Cu(Al,Ni) -matrix involve precipitation of $AlFe_3$ particles which withdraw some amount of aluminum from the matrix and thus increase the SFE with simultaneous increasing the twinning onset stress so that dislocation gliding becomes a dominating deformation mechanism.

It was noted above that both bronze and steel grains had their microhardnesses increased with the amount of SS introduced into the melted pool. Such a finding allows proposing that these grains experience dispersion hardening by the precipitates as described above. The steel grains were reinforced by the rod-like β′/AlNi precipitates as well as

even smaller ones found close to the grain boundaries. The bronze grains may be dispersion hardened by the fine coherent $AlFe_3$ $κ_{iv}$-phase precipitates (Fig. 4i, g).

5 Conclusions

Structurally homogeneous composites have been prepared by intermixing aluminum bronze and austenitic stainless steel in the melted pool formed by electron beam during additive manufacturing.

– The intermixing of the melted metals allowed obtaining solidified microstructures composed of ferrite and nickel aluminum bronze grains. Such a structural evolution was the result of redistribution of elements among the solidified components so that nickel atoms migrated to aluminum bronze and alloyed it so that it then solidified as nickel aluminum bronze. The nickel depleted austenite grains were correspondingly transformed into ferrite ones during cooling.
– The microhardness numbers of both ferrite and aluminum bronze grains increased with the content of stainless steel introduced into the composite. Such a hardening was due to precipitation of dispersed particles inside them, which formed from the dissolved alloys elements.
– Ferrite grains were reinforced by the core–shell β′/AlNi precipitates, while nickel aluminum bronze ones contained fine and coherent $AlFe_3$ $κ_{iv}$-phase precipitates so that the microhardness number difference between the bronze and steel grains was within the 0.4–0.5 GPa range. Such hardening resulted in reducing the ductility and simultaneously increasing the tensile strength of the samples.
– The tensile strength of the composites increased with the content of steel. Almost no tensile strength anisotropy was observed because of forming uniformly distributed grain structures. The bronze matrix demonstrated a combined dislocation/twinning deformation mechanism while steel grains contained almost no dislocations.
– Future work will be focused on obtaining more homogeneous structures of the composites and correspondingly, better combinations of strength and plasticity, by varying the deposition process parameters and characterizing the composites for corrosion and wear resistances.

Data availability All data generated or analysed during this study are included in this published article.

Declarations

Conflict of interest On behalf of all authors, the corresponding author states that there is no conflict of interest.

References

1. Shakor P, Chu SH, Puzatova A (2021) Dini E (2022) review of binder jetting 3D printing in the construction industry. Prog Addit Manuf 74(7):643–669. https://doi.org/10.1007/S40964-021-00252-9
2. Kucita P, Wang SC, Li WS et al (2019) The effects of substrate dilution on the microstructure and wear resistance of PTA Cu-Al-Fe aluminium bronze coatings. Wear 440–441:203102. https://doi.org/10.1016/j.wear.2019.203102
3. Lu SL, Meenashisundaram GK, Wang P et al (2020) The combined influence of elevated pre-sintering and subsequent bronze infiltration on the microstructures and mechanical properties of 420 stainless steel additively manufactured via binder jet printing. Addit Manuf 34:101266. https://doi.org/10.1016/j.addma.2020.101266
4. Rahni MRM, Beidokhti B, Haddad-Sabzevar M (2017) Effect of filler metal on microstructure and mechanical properties of manganese–aluminum bronze repair welds. Trans Nonferrous Met Soc China 27:507–513. https://doi.org/10.1016/S1003-6326(17)60057-8
5. Kalinin GM, Krestnikov NS, Jarovinskiy YL et al (2008) Microstructure investigation of bronze/steel brazed joints proposed for HHF components of ITER manufacturing. Fusion Eng Des 83:1521–1523. https://doi.org/10.1016/j.fusengdes.2008.06.030
6. Dong L, Chen W, Hou L et al (2016) Metallurgical process analysis and microstructure characterization of the bonding interface of QAl9–4 aluminum bronze and 304 stainless steel composite materials. J Mater Process Technol 238:325–332. https://doi.org/10.1016/j.jmatprotec.2016.07.041
7. Dharmendra C, Rice KP, Amirkhiz BS, Mohammadi M (2021) Atom probe tomography study of κ-phases in additively manufactured nickel aluminum bronze in as-built and heat-treated conditions. Mater Des 202:109541. https://doi.org/10.1016/j.matdes.2021.109541
8. Ma J, Fan C, Sun Q et al (2021) Tribological behavior of NiAl-based intermetallic compounds in artificial seawater. Tribol Int 153:106612. https://doi.org/10.1016/j.triboint.2020.106612
9. Kwarciak J, Bojarski Z, Morawiec H (1986) Phase transformation in martensite of Cu-12.4% Al. J Mater Sci 21:788–792. https://doi.org/10.1007/BF01117355
10. Adorno AT, Guerreiro MR, Benedetti AV (2001) Isothermal aging kinetics in the Cu–19 at.% Al alloy. J Alloys Compd 315:150–157. https://doi.org/10.1016/S0925-8388(00)01268-8
11. Dharmendra C, Hadadzadeh A, Amirkhiz BS et al (2019) Microstructural evolution and mechanical behavior of nickel aluminum bronze Cu-9Al-4Fe-4Ni-1Mn fabricated through wire-arc additive manufacturing. Addit Manuf 30:100872. https://doi.org/10.1016/j.addma.2019.100872
12. Gavrilova RVL, Petkov RI (2013) Researches on the structure and properties of heat treated, nickel alloyed, molybdenum modified aluminum bronze. Bulg Chem Commun 45:644–648
13. Wharton JA, Barik RC, Kear G et al (2005) The corrosion of nickel–aluminium bronze in seawater. Corros Sci 47:3336–3367. https://doi.org/10.1016/j.corsci.2005.05.053
14. Qin Z, Luo Q, Zhang Q et al (2018) Improving corrosion resistance of nickel-aluminum bronzes by surface modification with chromium ion implantation. Surf Coat Technol 334:402–409. https://doi.org/10.1016/j.surfcoat.2017.11.066
15. Makarenko K, Dubinin O, Shornikov P, Shishkovsky I (2020) Specific aspects of the transitional layer forming in the aluminium bronze—stainless steel functionally graded structures after laser metal deposition. Procedia CIRP 94:346–351. https://doi.org/10.1016/j.procir.2020.09.143
16. Li B, Han C, Lim CWJ, Zhou K (2022) Interface formation and deformation behaviors of an additively manufactured nickel-aluminum-bronze/15–5 PH multimaterial via laser-powder directed energy deposition. Mater Sci Eng A 829:142101. https://doi.org/10.1016/j.msea.2021.142101
17. Osipovich KS, Astafurova EG, Chumaevskii AV et al (2020) Gradient transition zone structure in "steel–copper" sample produced by double wire-feed electron beam additive manufacturing. J Mater Sci 55:9258–9272. https://doi.org/10.1007/s10853-020-04549-y
18. Khoroshko E, Filippov A, Tarasov S et al (2020) Strength and ductility improvement through thermomechanical treatment of wire-feed electron beam additive manufactured low stacking fault energy (SFE) aluminum bronze. Metals (Basel) 10:1–18. https://doi.org/10.3390/met10121568
19. Filippov A, Shamarin N, Moskvichev E et al (2022) The effect of heat input, annealing, and deformation treatment on structure and mechanical properties of electron beam additive manufactured (EBAM) silicon bronze. Mater 15:320915–3209. https://doi.org/10.3390/MA15093209
20. Zykova A, Chumaevskii A, Vorontsov A et al (2022) Evolution of microstructure and properties of Fe-Cu, manufactured by electron beam additive manufacturing with subsequent friction stir processing. Mater Lett. https://doi.org/10.1016/j.matlet.2021.131023
21. Meigh HJ (2018) Cast and wrought aluminium bronzes: properties, processes and structure. Cast Wrought Alum Bronzes. https://doi.org/10.1201/9781315138848
22. Prokoshkina D, Esin VA, Divinski SV (2017) Experimental evidence for anomalous grain boundary diffusion of Fe in Cu and Cu-Fe alloys. Acta Mater 133:240–246. https://doi.org/10.1016/j.actamat.2017.05.024
23. Raghavan V (2005) Al-Cu-Fe (Aluminum-Copper-Iron). J Phase Equilibria Diffus 261(26):59–64. https://doi.org/10.1007/S11669-005-0061-0
24. Tao XP, Zhang S, Zhang CH et al (2018) Effect of Fe and Ni contents on microstructure and wear resistance of aluminum bronze coatings on 316 stainless steel by laser cladding. Surf Coat Technol 342:76–84. https://doi.org/10.1016/j.surfcoat.2018.02.032
25. Sabzi HE, Maeng S, Liang X et al (2020) Controlling crack formation and porosity in laser powder bed fusion: alloy design and process optimisation. Addit Manuf 34:101360. https://doi.org/10.1016/j.addma.2020.101360
26. Kainuma R, Liu XJ, Ohnuma I et al (2005) Miscibility gap of B2 phase in NiAl to Cu₃Al section of the Cu–Al–Ni system. Intermetallics 13:655–661. https://doi.org/10.1016/j.intermet.2004.10.005